INTERNATIONAL JOURNAL FOR NUMERICAL METHODS IN FLUIDS
Int. J. Numer. Meth. Fluids 2010; **62**:1181–1208
DOI: 10.1002/fld.2054

A two-step Taylor-characteristic-based Galerkin method for incompressible flows and its application to flow over triangular cylinder with different incidence angles

Yan Bao, Dai Zhou*,† and Yao-Jun Zhao

School of Naval Architecture, Ocean and Civil Engineering, Shanghai Jiao Tong University,
No. 800 Dongchuan Road, Shanghai, China

SUMMARY

An alternative characteristic-based scheme, the two-step Taylor-characteristic-based Galerkin method is developed based on the introduction of multi-step temporal Taylor series expansion up to second order along the characteristic of the momentum equation. Contrary to the classical characteristic-based split (CBS) method, the current characteristic-based method does not require splitting the momentum equation, and segregate the calculation of the pressure from that of the velocity by using the momentum–pressure Poisson equation method. Some benchmark problems are used to examine the effectiveness of the proposed algorithm and to compare with the original CBS method, and the results show that the proposed method has preferable accuracy with less numerical dissipation.

We further applied the method to the numerical simulation of flow around equilateral triangular cylinder with different incidence angles in free stream. In this numerical investigation, the flow simulations are carried out in the low Reynolds number range. Instantaneous streamlines around the cylinder are used as a means to visualize the wake region behind, and they clearly show the flow pattern around the cylinder in time. The influence of incidence angle on flow characteristic parameters such as Strouhal number, Drag and Lift coefficients are discussed quantitatively. Copyright © 2009 John Wiley & Sons, Ltd.

Received 6 August 2008; Revised 23 February 2009; Accepted 26 February 2009

KEY WORDS: CBS; split error; characteristic-based Galerkin method; laminar flow; triangular cylinder; incidence angle

---

*Correspondence to: Dai Zhou, School of Naval Architecture, Ocean and Civil Engineering, Shanghai Jiao Tong University, No. 800 Dongchuan Road, Shanghai, China.

†E-mail: zhoudai@sjtu.edu.cn

Contract/grant sponsor: Key Project Foundation of Science and Technology Development of Shanghai; contract/grant number: 07JC14023
Contract/grant sponsor: National Natural Science Foundation of China; contract/grant number: 50778111

1. INTRODUCTION

In FEM, as well as in FDM and FVM, it is well known that the numerical solution of incompressible fluid dynamic problems with the conventional Galerkin method leads to spurious oscillatory due to two main sources. The first source is due to the convective character of the governing equations, which induces spurious oscillations primarily in the velocity field, particularly in the convection-dominated flows. The second source of instability is due to the mixed character of the incompressible Navier–Stokes equations, which induces oscillations primarily in the pressure field, as using inappropriate interpolation functions to approximate the velocity and pressure.

In order to overcome these instabilities, various stabilized finite element formulations have been developed in the past decades. To circumvent the restriction imposed by the LBB condition, the algorithms such as the pressure-stabilized Petrov–Galerkin (PSPG) formulation [1, 2], Galerkin least-square techniques (GLS) [3] and the finite increment calculus (FIC) [4] have been found to be among the most powerful tools. The formulation of PSPG method is achieved by adding to the Galerkin formulation of incompressible constraint equation a series of integrals of the residual of the momentum equation over element domains, while the procedures based on GLS work by introducing a Laplacian of pressure term in the mass balance equation. In the FIC procedure, application of classical Galerkin method to the modified differential equations for momentum and mass balance, which incorporate naturally the necessary stabilization terms, leads to a stabilized discrete system of equations. Recently, Codina and Blasco [5] have presented a new stabilized formulation for the transient incompressible N–S equations. The main idea of them is to introduce the projection gradient on the velocity space and to add to the continuity equation the difference between the Laplacian of the pressure and the divergence of this new unknown vector.

Strategies to cope with the convective effects arising in convection-dominated flows have also been extensively investigated in the last decades, such as the streamline–upwind/Galerkin method [6], space–time Galerkin/least-square method [7], subgrid scale method [8] and the Taylor–Galerkin method [9]. All these methods suppress spurious oscillations efficiently, by adding a stabilizing term to the original Galerkin formulation of the governing equation of the problem. The introduction of the characteristic Galerkin (CG) method of dealing with convection-dominated problems, originally presented in [10], contributes to discretize the particle time derivatives along the characteristic instead of the spatial time derivative, such that the convective terms disappear and the problem is that of simple diffusion for which the standard Galerkin approximation is optimal in the energy norm sense. In order to avoid the difficulties of complex programming and time consuming, which is arising in the original CG method, Zienkiewicz and Codina [11] derived an alternative version of the CG method by using a local Taylor expansion to approximate the unknown along the characteristics and also extended the split, which follows the process initially introduced by Chorin [12] and Témam [13], to the CG procedure, and that results in the well-known characteristic-based split (CBS) algorithm widely used in solution of the Navier-Stokes equation.

Since the introduction by Zienkiewicz and Codina, rapid progress is observed in the development of the CBS method in recent years [11, 14–25]. Simultaneously, the CBS scheme and its extension have been applied widely for the solution of fluid and solid dynamic problems encountered in engineering, including general compressible and incompressible flows [22, 26–30], turbulent flows [18, 31], shallow-water flows [14, 32], thermal flows [33, 34], porous medium flows [35–38], viscoelastic flows [39], solid dynamics [40] and bulk metal forming [41]. However, the application of the CBS algorithm to the flow over triangular cylinder with different incidences, which has fundamental fluid mechanics interest with respect to many technical applications, is not yet found in the existing literature, and that motivates us to numerically simulate this problem by using the characteristic-based method.

In terms of computational cost, as pressure segregation method, the fractional step schemes as well as other techniques based on the solution of a pressure Poisson equation and predictor–multicorrector algorithms are more attractive, since in these methods the computations of the velocity and the pressure are decoupled and then only scalar equations are need to be solved [42]. On the other hand, it was concluded by Guermond and Quartapelle [43] that to avoid the LBB condition in the fractional step algorithm with the same order interpolation approximations for velocity and pressure, only the non-incremental version (first order in time) of the algorithm can be used with the time step size larger than a critical one. By this reason, the splitting error introduced in the CBS method effects the overall accuracy and causes the temporal accuracy of the method to be of first order. For eliminating the first-order error in time caused by the split, Nithiarasu and Zienkiewicz [23] have proposed the explicit and matrix-free CBS schemes that have been proved, via some examples of benchmark flow problem, to be of second-order accuracy in time and approximate second order in spatial dimensions on unstructured meshes, and have also introduced the pressure stabilization technique into the proposed scheme so that the spurious pressure oscillation is alleviated obviously.

In this paper, an alternative version of the characteristic-based algorithm is proposed for finite element solutions of incompressible Navier–Stokes equations. The two-step second-order Taylor expansion is used in the time discretization of the transient convection–diffusion equation along its characteristic and, then, we extend the scheme to the Navier–Stokes equations and obtain the two-step Taylor-characteristic-based Galerkin scheme, abbreviated as the TCBG in the remainder of this paper. The segregation of the pressure calculation is implemented by solving the pressure Poisson equation, which is obtained by taking the divergence on both sides of the Crank–Nicolson formulation of the semi-discretized momentum equations, associated with the introduction of the incompressible constraint of the current time step. The key properties of the two-step TCBG scheme are that it is free from the splitting error, which will arise in the classical CBS method, and its second-order accuracy in time, and as in the classical CBS method, the same order interpolation for the velocity and pressure approximation can be used in the proposed scheme with no need for stabilization of pressure.

The organization of the paper is as follows. After describing the governing equations and the CBS scheme for incompressible flow in the next section, we present in detail the two-step TCBG scheme in Section 3. In Section 4, we validate and compare the approach with the CBS scheme through the numerical simulations of some benchmark problems. Section 5 is devoted to the application of the developed method to the numerical analysis of flow past triangular cylinder at different incidence angles. The influence of incidence angle on flow pattern around triangular cylinder and some characteristic flow parameters such as Drag and Lift coefficients and Strouhal number is also discussed. Section 6 concludes the paper with some conclusions.

2. GOVERNING EQUATIONS AND THE CBS SCHEME

2.1. Governing equations for incompressible viscous flow

The governing equations of unsteady incompressible viscous fluid flow can be expressed by the Navier–Stokes equations and continuity equation and written in the Eulerian form as follows:

$$\rho\left(\frac{\partial u_i}{\partial t}+u_j\frac{\partial u_i}{\partial x_j}\right)=-\frac{\partial p}{\partial x_i}+\frac{\partial \tau_{ij}}{\partial x_j} \quad \text{in } \Omega\times[0,T] \tag{1}$$

$$\frac{\partial u_i}{\partial x_i}=0 \quad \text{in } \Omega\times[0,T] \tag{2}$$

where Ω and $[0,T]$ are the spatial and temporal domains, u_i is the i-component velocity, t is time, ρ is the fluid density, p is the pressure. The deviatoric stresses are linked to the strain rates and given by

$$\tau_{ij}=2\mu\dot{\varepsilon}_{ij}=\mu\left(\frac{\partial u_i}{\partial x_j}+\frac{\partial u_j}{\partial x_i}\right) \tag{3}$$

where μ is the viscosity constant.

Using the following non-dimensionalized variables:

$$u_i^*=u_i/U_\infty,\quad x_i^*=x_i/D,\quad t^*=tU_\infty/D,\quad \rho^*=\rho/\rho_\infty,\quad p^*=p/\rho_\infty U_\infty^2,\quad Re=U_\infty D/v \tag{4}$$

where D is a characteristic length, U_∞ is a characteristic velocity, ρ_∞ is characteristic density and Re is the Reynolds number, v is kinematic viscosity equal to μ/ρ, the non-dimensionalized form of Equations (1) and (2) can be written as

$$\frac{\partial u_i^*}{\partial t^*}+u_j^*\frac{\partial u_i^*}{\partial x_j^*}=-\frac{\partial p^*}{\partial x_i^*}+\frac{1}{Re}\frac{\partial \tau_{ij}^*}{\partial x_j^*} \tag{5}$$

$$\frac{\partial u_i^*}{\partial x_i^*}=0 \tag{6}$$

where

$$\tau_{ij}^*=\frac{\partial u_i^*}{\partial x_j^*}+\frac{\partial u_j^*}{\partial x_i^*}$$

Dropping the asterisk from the non-dimensional variables for brevity, the non-dimensional equations for (1) and (2) can be rewritten as

$$\frac{\partial u_i}{\partial t}+u_j\frac{\partial u_i}{\partial x_j}=-\frac{\partial p}{\partial x_i}+\frac{1}{Re}\frac{\partial \tau_{ij}}{\partial x_j} \tag{7}$$

$$\frac{\partial u_i}{\partial x_i}=0 \tag{8}$$

The problem definition is completed by prescribing appropriate initial and boundary conditions.

2.2. The CBS scheme

In this subsection, we only give the essential steps of the CBS algorithm. The spatial Galerkin discretization procedure can be found in the classical reference of Zienkiewicz and Taylor [44], and is not described here. For every time increment Δt, the semi-implicit form of the CBS method for solving the governing equations perform in the following three steps:

(1) Solving the intermediate momentum equations

$$u_i^* = u_i^n - \Delta t \left(u_j^n \frac{\partial u_i^n}{\partial x_j} - \frac{1}{Re} \frac{\partial \tau_{ij}^n}{\partial x_j} \right) + \frac{\Delta t^2}{2} u_k^n \frac{\partial}{\partial x_k} \left(u_j^n \frac{\partial u_i^n}{\partial x_j} - \frac{1}{Re} \frac{\partial \tau_{ij}^n}{\partial x_j} \right) \tag{9}$$

(2) Calculating the pressure from the Poisson equation

$$\frac{\partial^2 p^{n+1}}{\partial x_i \partial x_i} = \frac{1}{\Delta t} \frac{\partial u_i^*}{\partial x_i} \tag{10}$$

(3) Performing velocity correction

$$u_i^{n+1} = u_i^* - \Delta t \frac{\partial p^{n+1}}{\partial x_i} + \frac{\Delta t^2}{2} u_k^n \frac{\partial}{\partial x_k} \left(\frac{\partial p^n}{\partial x_i} \right) \tag{11}$$

where u_i^* represents the auxiliary velocity.

3. TWO-STEP TCBG SCHEME

We first consider the time discretization of one-dimensional convective–diffusive equation, which is written as

$$\frac{\partial \phi}{\partial t} + U \frac{\partial \phi}{\partial x} - \frac{\partial}{\partial x} \left(k \frac{\partial \phi}{\partial x} \right) + Q = 0 \tag{12}$$

In the above equation ϕ is a concentration being transported by the velocity U in a convective manner or by diffusion action, k is the diffusion coefficient, the term Q represents any external sources of the quantity ϕ. Making a Taylor expansion in time to second-order accuracy, the formulation of the above Equation (12) along the characteristic in two steps can be written as

$$\begin{aligned} \phi^{n+1/2} &= \phi^n|_{x-\delta_1/2} + \frac{\Delta t}{2} \left(\frac{\partial}{\partial x} \left(k \frac{\partial \phi}{\partial x} \right) - Q \right)^n \Bigg|_{x-\delta_1/2} \\ \phi^{n+1} &= \phi^n|_{x-\delta_2} + \Delta t \left(\frac{\partial}{\partial x} \left(k \frac{\partial \phi}{\partial x} \right) - Q \right)^{n+1/2} \Bigg|_{x-\delta_2/2} \end{aligned} \tag{13}$$

where δ_1 and δ_2 are the distances traveled, during time interval of Δt, by the particles X_1 and X_2 along the x-axis at average velocity $\bar{U}_1$ and $\bar{U}_2$, respectively (see Figure 1), and are calculated by

$$\delta_1 = \bar{U}_1 \Delta t, \quad \delta_2 = \bar{U}_2 \Delta t \tag{14}$$

where the approximations for the average velocity of the particles along characteristics are given as follows:

$$\bar{U}_1 = \frac{U^{n+1/2} + U^n|_{x-\delta_1/2}}{2}, \quad \bar{U}_2 = U^{n+1/2}|_{x-\delta_2/2} \tag{15}$$

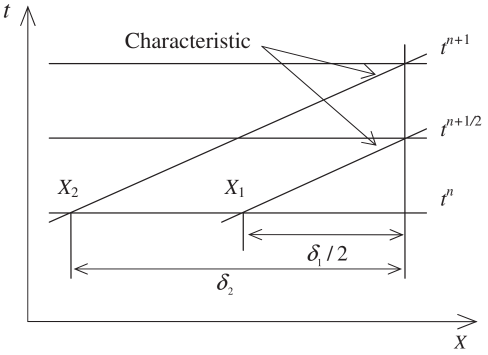

Figure 1. Two-step temporal discretization along the characteristics (two particles X_1 and X_2 and their corresponding trajectories).

with

$$U^{n+1/2} = U^n + O(\Delta t) \tag{16}$$

In order to circumvent the difficulty of mesh updating, which arises in the original characteristic-based method, using the Taylor expansion we have the following:

$$\phi^n|_{x-\delta_1/2} = \phi^n - \frac{\delta_1}{2}\frac{\partial \phi^n}{\partial x} + \frac{\delta_1^2}{8}\frac{\partial^2 \phi^n}{\partial x^2} + O(\Delta t^3), \quad \phi^n|_{x-\delta_2} = \phi^n - \delta_2 \frac{\partial \phi^n}{\partial x} + \frac{\delta_2^2}{2}\frac{\partial^2 \phi^n}{\partial x^2} + O(\Delta t^3) \tag{17}$$

$$\begin{aligned} U^n|_{x-\delta_1/2} &= U^n - U^n \frac{\Delta t}{2}\frac{\partial U^n}{\partial x} + O(\Delta t^2) \\ U^{n+1/2}|_{x-\delta_2/2} &= U^{n+1/2} - U^{n+1/2}\frac{\Delta t}{2}\frac{\partial U^{n+1/2}}{\partial x} + O(\Delta t^2) \end{aligned} \tag{18}$$

$$\begin{aligned} \left(\frac{\partial}{\partial x}\left(k\frac{\partial \phi}{\partial x}\right) - Q\right)^n \Bigg|_{x-\delta_1/2} &= \left(\frac{\partial}{\partial x}\left(k\frac{\partial \phi}{\partial x}\right) - Q\right)^n - \frac{\delta_1}{2}\frac{\partial}{\partial x}\left(\frac{\partial}{\partial x}\left(k\frac{\partial \phi}{\partial x}\right) - Q\right)^n + O(\Delta t^2) \\ \left(\frac{\partial}{\partial x}\left(k\frac{\partial \phi}{\partial x}\right) - Q\right)^{n+1/2} \Bigg|_{x-\delta_2/2} &= \left(\frac{\partial}{\partial x}\left(k\frac{\partial \phi}{\partial x}\right) - Q\right)^{n+1/2} \\ &\quad - \frac{\delta_2}{2}\frac{\partial}{\partial x}\left(\frac{\partial}{\partial x}\left(k\frac{\partial \phi}{\partial x}\right) - Q\right)^{n+1/2} + O(\Delta t^2) \end{aligned} \tag{19}$$

Making use of Equations (14)–(19) and neglecting higher-order terms, the Equation (13) can be rewritten by

$$\begin{aligned} \phi^{n+1/2} = \phi^n &- \frac{\Delta t}{2}\left(U^n \frac{\partial \phi^n}{\partial x} - \frac{\partial}{\partial x}\left(k\frac{\partial \phi^n}{\partial x}\right) + Q^n\right) \\ &+ \frac{\Delta t^2}{8} U^n \frac{\partial}{\partial x}\left(U^n \frac{\partial \phi^n}{\partial x} - 2\left(\frac{\partial}{\partial x}\left(k\frac{\partial \phi^n}{\partial x}\right) - Q^n\right)\right) \end{aligned} \tag{20}$$

$$\phi^{n+1} = \phi^n - \Delta t\left(U^{n+1/2}\frac{\partial \phi^n}{\partial x} - \frac{\partial}{\partial x}\left(k\frac{\partial \phi^{n+1/2}}{\partial x}\right) + Q^{n+1/2}\right)$$
$$+\frac{\Delta t^2}{2}U^{n+1/2}\frac{\partial}{\partial x}\left(U^{n+1/2}\frac{\partial \phi^n}{\partial x} - \frac{\partial}{\partial x}\left(k\frac{\partial \phi^{n+1/2}}{\partial x}\right) + Q^{n+1/2}\right) \tag{21}$$

We can easily make extension of the procedures described above to vector variables, and then obtain the final forms of the two-step Taylor-characteristic-based scheme for the convective–diffusive equation, which can be expressed as

$$\phi^{n+1/2} = \phi^n - \frac{\Delta t}{2}\left(U_j^n\frac{\partial \phi^n}{\partial x_j} - \frac{\partial}{\partial x_i}\left(k\frac{\partial \phi^n}{\partial x_i}\right) + Q^n\right)$$
$$+\frac{\Delta t^2}{8}U_k^n\frac{\partial}{\partial x_k}\left(U_j^n\frac{\partial \phi^n}{\partial x_j} - 2\left(\frac{\partial}{\partial x_i}\left(k\frac{\partial \phi^n}{\partial x_i}\right) - Q^n\right)\right) \tag{22}$$

$$\phi^{n+1} = \phi^n - \Delta t\left(U_j^{n+1/2}\frac{\partial \phi^n}{\partial x_j} - \frac{\partial}{\partial x_i}\left(k\frac{\partial \phi^{n+1/2}}{\partial x_i}\right) + Q^{n+1/2}\right)$$
$$+\frac{\Delta t^2}{2}U_k^{n+1/2}\frac{\partial}{\partial x_k}\left(U_j^{n+1/2}\frac{\partial \phi^n}{\partial x_j} - \frac{\partial}{\partial x_i}\left(k\frac{\partial \phi^{n+1/2}}{\partial x_i}\right) + Q^{n+1/2}\right) \tag{23}$$

Applying the described method to the momentum equations, we yield the following scheme:

$$u_i^{n+1/2} = u_i^n - \frac{\Delta t}{2}\left(u_j^n\frac{\partial u_i^n}{\partial x_j} + \frac{\partial p^{n+\theta}}{\partial x_i} - \frac{1}{Re}\frac{\partial \tau_{ij}^n}{\partial x_j}\right)$$
$$+\frac{\Delta t^2}{8}u_k^n\frac{\partial}{\partial x_k}\left(u_j^n\frac{\partial u_i^n}{\partial x_j} + 2\left(\frac{\partial p^{n+\theta}}{\partial x_i} - \frac{1}{Re}\frac{\partial \tau_{ij}^n}{\partial x_j}\right)\right) \tag{24}$$

$$u_i^{n+1} = u_i^n - \Delta t\left(u_j^{n+1/2}\frac{\partial u_i^n}{\partial x_j} + \frac{\partial p^{n+\theta}}{\partial x_i} - \frac{1}{Re}\frac{\partial \tau_{ij}^{n+1/2}}{\partial x_j}\right)$$
$$+\frac{\Delta t^2}{2}u_k^{n+1/2}\frac{\partial}{\partial x_k}\left(u_j^{n+1/2}\frac{\partial u_i^n}{\partial x_j} + \frac{\partial p^{n+\theta}}{\partial x_i} - \frac{1}{Re}\frac{\partial \tau_{ij}^{n+1/2}}{\partial x_j}\right) \tag{25}$$

where $\theta \in [0, 1]$ with $\theta = 0$ for explicit forms, $0 < \theta < 1$ for semi-explicit forms and $\theta = 1$ for fully implicit forms, and particularly; we set $\theta = 0$ and $\theta = 1$ in Equations (24) and (25), respectively.

The spatial discretization of Equations (24) and (25) is performed by using the standard Galerkin procedure after the temporal discretization. The primitive unknown variables, u_i and p, are spatially approximated by the Galerkin finite element shape functions of the same order as

$$u_i = \sum_I \Phi_I u_{iI}, \quad p = \sum_I \Phi_I p_I \tag{26}$$

in which u_{iI}, p_I are nodal quantities, the subscript I represents an element node and Φ_I the nodal shape function at node I.

Multiplying the semi-discrete equations by weighting functions and integrating over computational domain, the resulting finite element algebraic equations can be expressed as follows:

$$M_{IJ}\frac{u_{iJ}^{n+1/2} - u_{iJ}^{n}}{\Delta t/2} = -N_{IJ}^{n} u_{iJ}^{n} - S_{iI}^{n} - G_{iIJ} p_J^{n} - \frac{\Delta t}{4}(C_{IJ}^{n} u_{iJ}^{n} + 2F_{iIJ}^{n} p_J^{n}) + L_{iI}^{n} \tag{27}$$

$$\begin{aligned} M_{IJ}\frac{u_{iJ}^{n+1} - u_{iJ}^{n}}{\Delta t} &= -N_{IJ}^{n+1/2} u_{iJ}^{n} - S_{iI}^{n+1/2} - G_{iIJ} p_J^{n+1} \\ &\quad - \frac{\Delta t}{2}(C_{IJ}^{n+1/2} u_{iJ}^{n} + F_{iIJ}^{n+1/2} p_J^{n+1}) + L_{iI}^{n+1/2} \end{aligned} \tag{28}$$

As we use linear finite element shape functions, the higher-order terms are neglected in the above equations. The elemental matrices and vectors arising in Equations (27)–(28) are given as follows:

$$\begin{aligned} M_{IJ} &= \int_{\Omega^e} \Phi_I \Phi_J \,\mathrm{d}\Omega, \quad G_{iIJ} = \int_{\Omega^e} \Phi_I \frac{\partial \Phi_J}{\partial x_i}\,\mathrm{d}\Omega \\ N_{IJ}^{n+\theta} &= \int_{\Omega^e} \Phi_I u_j^{n+\theta} \frac{\partial \Phi_J}{\partial x_j}\,\mathrm{d}\Omega, \quad F_{iIJ}^{n+\theta} = \int_{\Omega^e} \frac{\partial \Phi_I}{\partial x_k} u_k^{n+\theta} \frac{\partial \Phi_J}{\partial x_i}\,\mathrm{d}\Omega \\ S_{iI}^{n+\theta} &= \frac{1}{Re}\int_{\Omega^e} \frac{\partial \Phi_I}{\partial x_j}\left(\frac{\partial u_i^{n+\theta}}{\partial x_j} + \frac{\partial u_j^{n+\theta}}{\partial x_i}\right)\mathrm{d}\Omega, \quad C_{IJ}^{n+\theta} = \int_{\Omega^e} \frac{\partial \Phi_I}{\partial x_k} u_k^{n+\theta} u_j^{n+\theta} \frac{\partial \Phi_J}{\partial x_j}\,\mathrm{d}\Omega \\ L_{iI}^{n+\theta} &= \frac{1}{Re}\int_{\Gamma^e} \Phi_I \left(\frac{\partial u_i^{n+\theta}}{\partial x_j} + \frac{\partial u_j^{n+\theta}}{\partial x_i}\right) n_j \,\mathrm{d}\Gamma \end{aligned} \tag{29}$$

where $\theta = 0, \frac{1}{2}$, and we denote node indices with subscripts I, J, space indices with subscripts i, j, k, and a repeated index means summation.

Before the calculation of Equation (28), the pressure at the $n+1$ time step has to be solved for a given velocity at the previous time step, and then it is necessary to derive the pressure Poisson equation equivalent to the continuity equation. The pressure Poisson equation is obtained by taking the divergence of the semi-discrete Crank–Nicolson scheme of the momentum equation and is written as

$$\frac{\partial^2 p^{n+1}}{\partial x_i \partial x_i} = \frac{1}{\Delta t}\frac{\partial}{\partial x_i}(u_i^{n} - u_i^{n+1}) - \frac{\partial}{\partial x_i}\left(u_j^{n+1/2}\frac{\partial u_i^{n+1/2}}{\partial x_j} - \frac{1}{Re}\frac{\partial \tau_{ij}^{n+1/2}}{\partial x_j}\right) \tag{30}$$

and applying the incompressibility condition at the $n+1$ time level leads to the following equation:

$$\frac{\partial^2 p^{n+1}}{\partial x_i \partial x_i} = \frac{1}{\Delta t}\frac{\partial u_i^n}{\partial x_i} - \frac{\partial}{\partial x_i}\left(u_j^{n+1/2}\frac{\partial u_i^{n+1/2}}{\partial x_j} - \frac{1}{Re}\frac{\partial \tau_{ij}^{n+1/2}}{\partial x_j}\right) \tag{31}$$

By using the Galerkin approximation, the weak formulation of the Equation (31) is obtained as

$$\begin{aligned}\int_\Omega \frac{\partial \Phi}{\partial x_j}\frac{\partial p^{n+1}}{\partial x_j}\,\mathrm{d}\Omega = & -\frac{1}{\Delta t}\int_\Omega \Phi\frac{\partial u_i^n}{\partial x_i}\,\mathrm{d}\Omega - \int_\Omega \frac{\partial \Phi}{\partial x_i}\left(u_j^{n+1/2}\frac{\partial u_i^{n+1/2}}{\partial x_j} - \frac{1}{Re}\frac{\partial \tau_{ij}^{n+1/2}}{\partial x_j}\right)\mathrm{d}\Omega \\ & + \int_\Gamma \Phi\left(u_j^{n+1/2}\frac{\partial u_i^{n+1/2}}{\partial x_j} - \frac{1}{Re}\frac{\partial \tau_{ij}^{n+1/2}}{\partial x_j} + \frac{\partial p^{n+1}}{\partial x_i}\right) n_i\,\mathrm{d}\Gamma\end{aligned} \tag{32}$$

Making use of Equation (30), the boundary integration part in the right-hand side of Equation (32) can be expressed as

$$\int_\Gamma \Phi\left(u_j^{n+1/2}\frac{\partial u_i^{n+1/2}}{\partial x_j} - \frac{1}{Re}\frac{\partial \tau_{ij}^{n+1/2}}{\partial x_j} + \frac{\partial p^{n+1}}{\partial x_i}\right) n_i\,\mathrm{d}\Gamma = \frac{1}{\Delta t}\int_\Gamma \Phi(u_i^n - u_i^{n+1})n_i\,\mathrm{d}\Gamma \tag{33}$$

Substituting Equation (33) into (32), we can yield

$$\begin{aligned}\int_\Omega \frac{\partial \Phi}{\partial x_j}\frac{\partial p^{n+1}}{\partial x_j}\,\mathrm{d}\Omega = & -\frac{1}{\Delta t}\int_\Omega \Phi\frac{\partial u_i^n}{\partial x_i}\,\mathrm{d}\Omega - \int_\Omega \frac{\partial \Phi}{\partial x_i}\left(u_j^{n+1/2}\frac{\partial u_i^{n+1/2}}{\partial x_j} - \frac{1}{Re}\frac{\partial \tau_{ij}^{n+1/2}}{\partial x_j}\right)\mathrm{d}\Omega \\ & + \frac{1}{\Delta t}\int_\Gamma \Phi(u_i^n - u_i^{n+1})n_i\,\mathrm{d}\Gamma\end{aligned} \tag{34}$$

For most cases, the value of u_i^{n+1} over the outlet boundary is assumed to be unknown; for this reason, we can approximate u_i^{n+1} by $2u_i^{n+1/2} - u_i^n$.

Further, the final finite element formulation of the pressure Poisson equation in the matrix vector form can be written as

$$H_{IJ}\,p_J^{n+1} = -Q_{iIJ}\,u_{iJ}^n - R_{iIJ}\,u_{iJ}^{n+1/2} + P_I \tag{35}$$

where the elemental matrices and vector are defined by

$$\begin{aligned} H_{IJ} &= \int_{\Omega^e}\frac{\partial \Phi_I}{\partial x_i}\frac{\partial \Phi_J}{\partial x_i}\,\mathrm{d}\Omega, \quad P_I = \frac{2}{\Delta t}\int_{\Gamma^e}\Phi_I(u_i^n - u_i^{n+1/2})n_i\,\mathrm{d}\Gamma \\ Q_{iIJ} &= \frac{1}{\Delta t}\int_{\Omega^e}\Phi_I\frac{\partial \Phi_J}{\partial x_i}\,\mathrm{d}\Omega, \quad R_{iIJ} = \int_{\Omega^e}\frac{\partial \Phi_I}{\partial x_i}u_j^{n+1/2}\frac{\partial \Phi_J}{\partial x_j}\,\mathrm{d}\Omega \end{aligned} \tag{36}$$

Now, the solution procedure of TCBG method for governing equations may be summarized as follows:

1. Solve Equation (27) explicitly for velocity field at $n+1/2$ time step $u_i^{n+1/2}$;
2. Calculate pressure field p^{n+1} from the Poisson-type equation (35);
3. Use Equation (28) to determine u_i^{n+1} once $u_i^{n+1/2}$ and p^{n+1} are known.

4. NUMERICAL VALIDATION AND COMPARISON OF THE TWO-STEP TCBG SCHEME

In this section, we apply the proposed method to numerically simulate some incompressible flow test cases and compare the results with the one obtained by using the CBS method. The tests include incompressible flow inside a lid-driven square cavity at $Re = 1000$, 5000 and unsteady flow past circular cylinder at $Re = 100$. In the following simulations, we have used equal-order velocity–pressure interpolation, particularly, for the cavity flow the bilinear quadrilateral element with structured mesh is used, while the linear triangular element with unstructured mesh is used for the computation of flow past cylinder problem.

4.1. Lid-driven cavity flow

The first example we consider is the classical cavity flow problem. The computational domain is the unit square, the enforced boundary conditions for the velocities and the pressure are as follows: the velocities are fixed to zero everywhere on boundaries except on the top of it, where the x- and y-velocity are prescribed to 1 and 0, respectively, and the pressure at the left bottom corner is prescribed to 0. For $Re = 1000$, the uniform grids with 21×21, 41×41 nodal points and globally distorted mesh (see Figure 2) with 40×40 elements are used, and for $Re = 5000$, two non-uniform meshes (refined near the boundaries) of 41×41 and 81×81 nodal points are used for the computation. To determine the accuracy of the schemes, we compare the numerical results with the reference data that are obtained by using the code developed for solution of two-dimensional steady incompressible flow by Erturk *et al.* with a fine uniform grid mesh of 256×256 (see [45]).

The streamline and pressure patterns for $Re = 5000$ obtained with mesh 81×81 and the TCBG are shown in Figure 3. The comparisons of x-velocity profiles along the cavity mid-section $x = 0.5$ for $Re = 1000$ and $Re = 5000$ are shown in Figures 4 and 5, respectively. It is observed from these

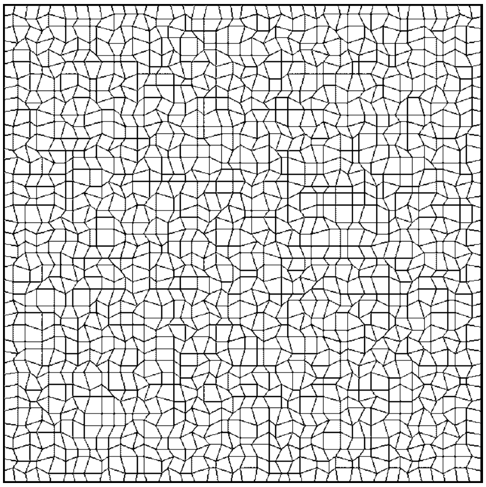

Figure 2. The computational mesh with global distortion (40×40 elements).

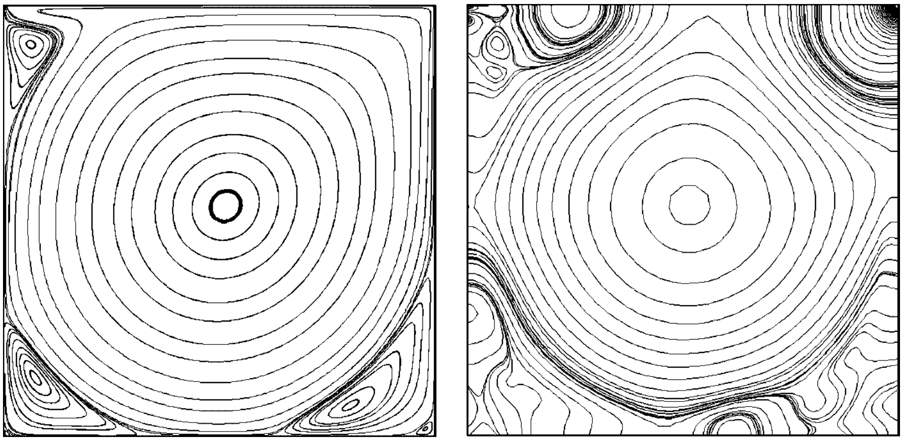

Figure 3. Streamline contour and pressure pattern for the driven cavity flow at $Re = 5000$ using the structured non-uniform mesh of 81×81 and the TCBG method.

figures that both schemes can result in good accuracy, especially for more fine meshes. It can be also observed from the results that the profiles obtained by the TCBG method are more close to the reference one than those obtained by the CBS.

The convergence behavior of the CBS and TCBG method to the steady states for $Re = 1000$ using different time step sizes is also shown in Figure 6. The steady-state convergence criteria ($<10^{-6}$) is based on the L_2 norm residual of the velocity normalized by the norm of the velocity at the current time step, and is expressed by

$$\sqrt{\sum_{i=1}^{\text{No. of nodes}} (|u|_i^{n+1} - |u|_i^n)^2} \Bigg/ \sqrt{\sum_{i=1}^{\text{No. of nodes}} (|u|_i^{n+1})^2} \tag{37}$$

It is observed that both CBS and TCBG display good behavior when using smaller time step size Δt equal to 0.01. However, at $\Delta t = 0.02$, CBS fails to reach the prescribed residual tolerance, whereas TCBG reaches the tolerance faster than that when using smaller time step of 0.01. The comparison of the results obtained using different schemes may indicate that the proposed method performs better than the CBS method, in this problem.

4.2. Flow past a circular cylinder

In the second example, we solve the benchmark problem of flow over a cylinder. The circular cylinder is of unit diameter and is placed in the region $\Omega = [-4.0, 12.0] \times [-4.0, 4.0]$. The center of the cylinder lies at the origin of Cartesian system, so that the inflow boundary is located 4.0 in front of the center of the cylinder and the outflow boundary 12.0 downstream of the center of the cylinder. The top and bottom boundaries are located 4.0 above and below the center of the cylinder. The boundary conditions are as below: at the inflow, the x- and y-velocity are described to 1 and 0, whereas at top and bottom boundaries the y-velocity component is prescribed to 0 and the x-component is left to free. At the outflow, both the x- and y-components are free. The

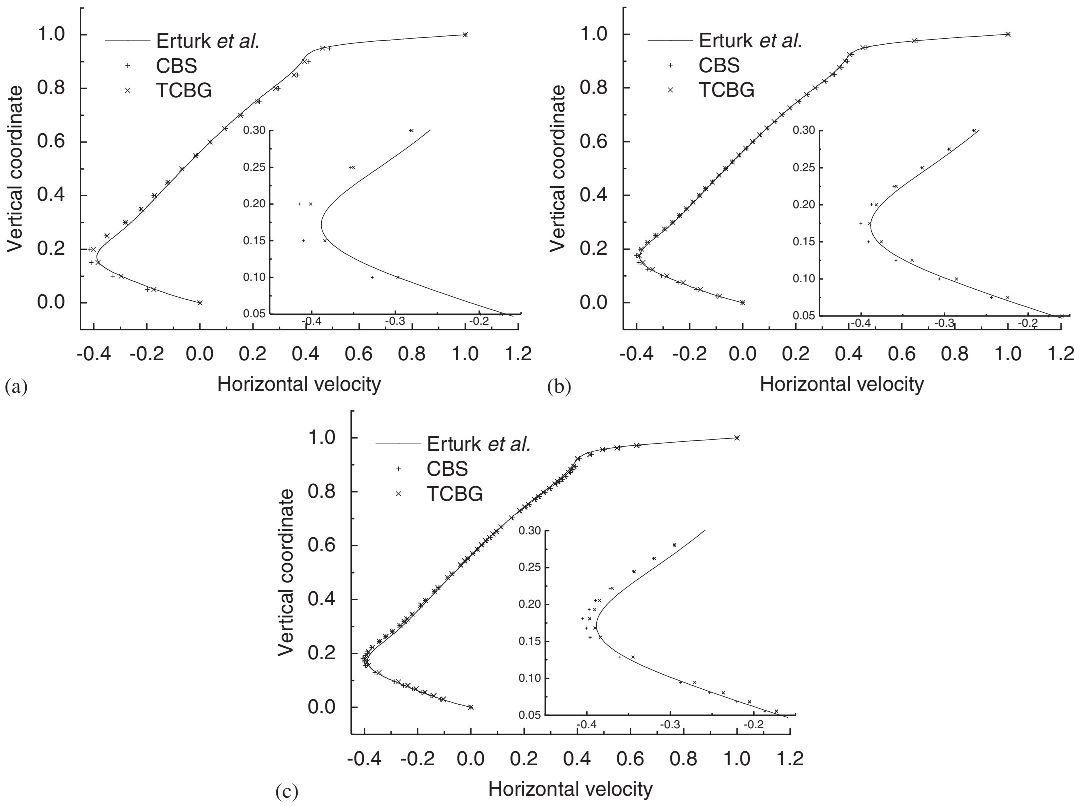

Figure 4. Velocity profiles along vertical section for a cavity flow at $Re=1000$ with different meshes and time step sizes. Closed view of the stationary point of the velocity is shown in the inset: (a) uniform mesh 21×21 ($\Delta t=0.04$); (b) uniform mesh 41×41 ($\Delta t=0.02$); and (c) distorted mesh 41×41 ($\Delta t=0.01$).

no-slip boundary condition is assumed on the cylinder surface. The Reynolds number based on the cylinder diameter and the free-stream velocity is 100.

Simulations have been performed on two finite element mesh systems, The first coarse mesh 1 consists of 2076 nodal points and 3972 elements, whereas the second fine mesh 2 consists of 9228 nodal points and 18 056 elements, both being refined while approaching the cylinder. The corresponding time step sizes for meshes 1 and 2 are 0.04 and 0.01, respectively.

Figure 7 shows computed x-component velocity contour and the pressure pattern using the second fine mesh and the TCBG method. The comparison of temporal evolution of y-component velocity at the midpoint of the outflow side, using the CBS and the TCBG method, is shown in Figure 8. It is observed from Figure 8(a) that the CBS method is slightly more dissipative than the TCBG method, with smaller frequency and amplitude, when using the coarse mesh 1 with larger time step size. However, in Figure 8(b), both results of CBS and TCBG become very similar for the fine mesh 2 with smaller time step size. This example serves as an evidence to demonstrate that even though both methods are accurate and suitable for the solution of incompressible flow, the TCBG method is more preferable for its less dissipative character when using larger time step size and coarse mesh grids.

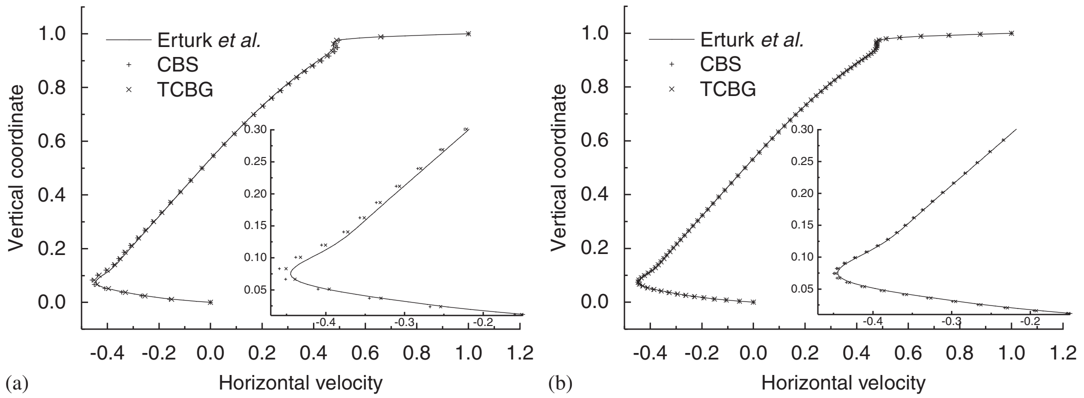

Figure 5. Velocity profiles along vertical section for a cavity flow at $Re = 5000$ using different meshes and time step sizes. Closed view of the stationary point of the velocity is shown in the inset: (a) non-uniform mesh 41×41 ($\Delta t = 0.01$) and (b) non-uniform mesh 81×81 ($\Delta t = 0.003$).

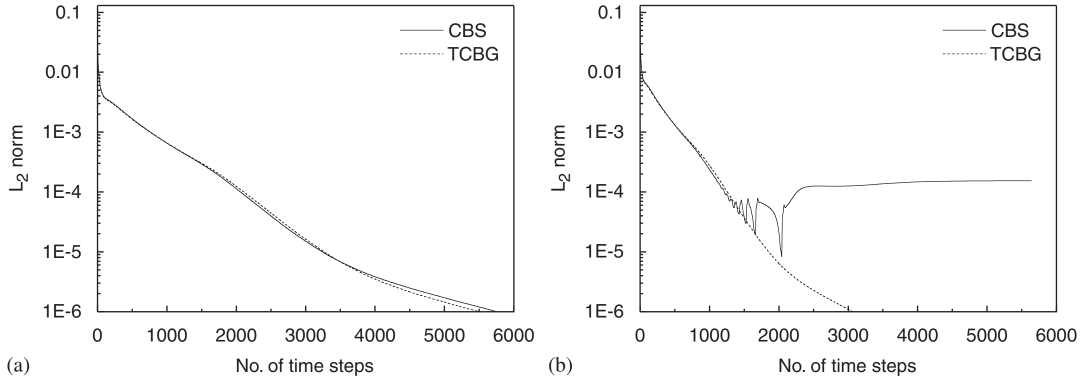

Figure 6. Convergence to the steady state for the lid-driven cavity flow at $Re = 1000$ using uniform mesh of 41×41 nodal points and different time step sizes: (a) $\Delta t = 0.01$ and (b) $\Delta t = 0.02$.

5. NUMERICAL APPLICATION ON THE FLOW PAST TRIANGULAR CYLINDER AT DIFFERENT INCIDENCE ANGLES

5.1. Statement of the problem

In this section, the developed two-step TCBG method is applied to perform numerical simulation of flow past equilateral triangular cylinder placed at different incidences ($0° \leqslant \alpha \leqslant 60°$, $\Delta\alpha = 7.5°$). The geometry of flow domain and boundary conditions are shown in Figure 9. The origin of the Cartesian system is located at the center point of cylinder. The cylinder is of unit side length and is placed in a rectangular computational domain whose upstream boundary is located at 13.1 side length from the center of the cylinder. The top and bottom of the domain are located at 15 side length from the center of the cylinder, such that we can impose free-stream boundary conditions at the top and bottom boundaries without noticeably affecting the solution. The downstream

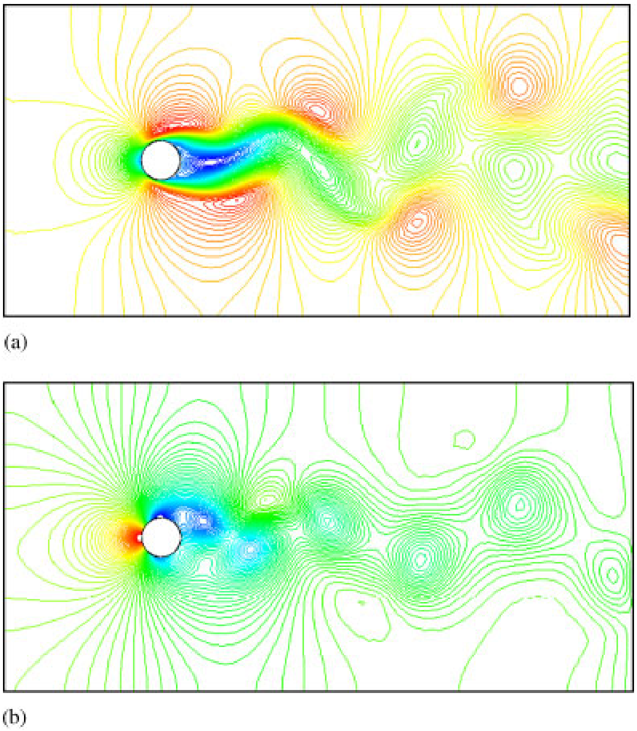

Figure 7. Contours of x-component velocity and pressure for the flow over a cylinder at $Re = 100$ using the TCBG method and the mesh consist of 18 056 triangle elements, with 9228 nodal points: (a) x-component velocity contour and (b) the pressure contour.

boundary is located at 25.5 side length from the center of the cylinder. The corresponding boundary conditions used in the present simulations are briefly mentioned here. At the inflow, top and bottom boundaries, the free-stream velocity U_∞ is specified to be unity and the vertical-component of the velocity is set to zero. The no-slip boundary condition is specified for the velocity on the cylinder surface. Pressure boundary condition is of Dirichlet type at the outflow boundary, $p = 0$. The time marching calculations were started with the fluid at rest and the free-stream velocity is gradually increased in time from zero to unity, according to a hyperbolic tangent distribution, i.e. $U_\infty(t) = \tanh(t)$.

5.2. *Definition of flow parameters*

Some flow parameters that are used to characterize flow behavior such as Drag and Lift coefficients and Strouhal number are defined as follows.

5.2.1. Drag and Lift coefficients. The non-dimensional Drag and Lift coefficients of the cylinder are defined by

$$C_\mathrm{D} = \frac{2F_\mathrm{D}}{\rho U_\infty D}, \quad C_\mathrm{L} = \frac{2F_\mathrm{L}}{\rho U_\infty D} \tag{38}$$

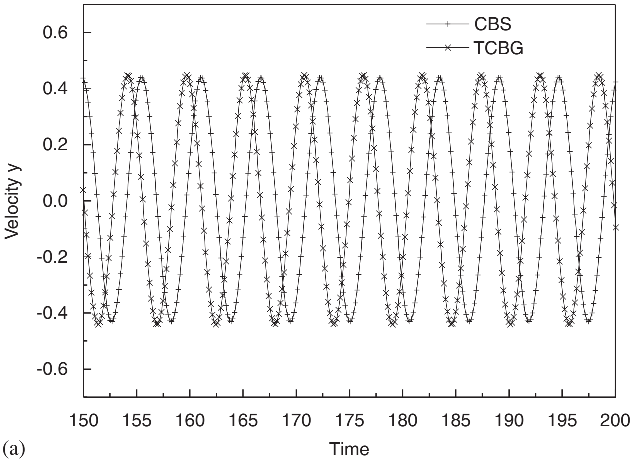

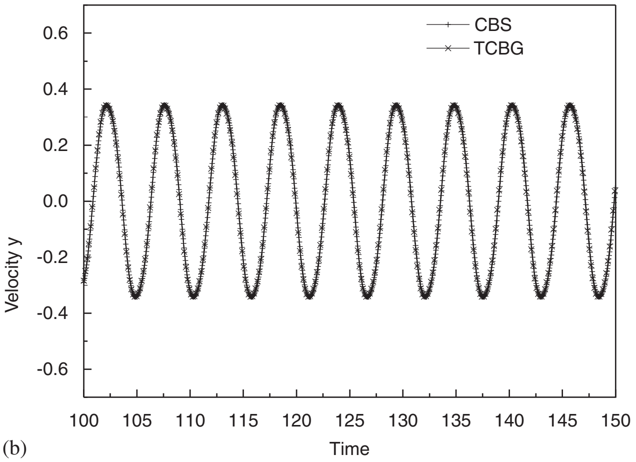

Figure 8. Temporal evolution of the y-velocity component at the point (12.0, 0.0): (a) using mesh 1 and (b) using mesh 2.

where F_{D} and F_{L} are respectively the Drag and Lift forces acting on the cylinder; the characteristic length D is taken to be the side length of the triangle.

5.2.2. Strouhal number. The dimensionless parameter, Strouhal number, is used to describe the frequency of the flow in the wake region and defined here as

$$St = f_{\mathrm{s}} D / U_{\infty} \tag{39}$$

where f_{s} is the vortex shedding frequency and computed from the periodic time variation of the Lift coefficient. Since U_{∞} and D are non-dimensionalized to be of unity for all cases examined, the Strouhal number is equivalent to the shedding frequency.

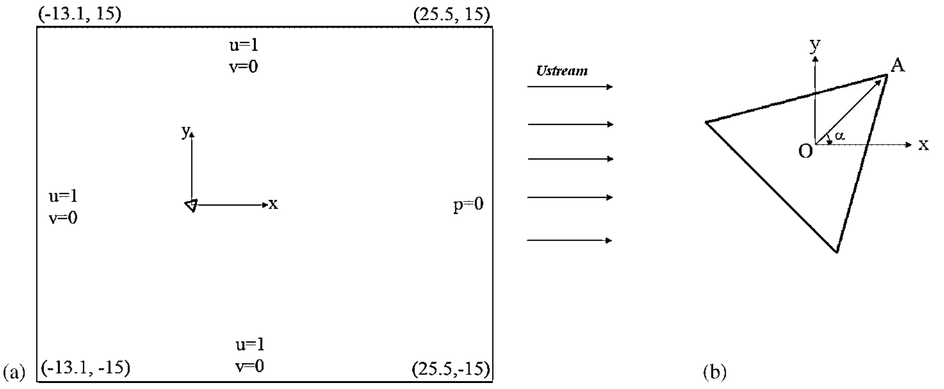

Figure 9. Flow past the equilateral triangular cylinder at different angles to the direction of flow: (a) computational domain and boundary conditions and (b) definition of incidence angle α, where the alpha angle is defined as the angle between the vector OA and the free-stream direction, and the point O is the central point of the cylinder, the point A is the vertex of the cylinder.

5.3. Numerical results and discussions

In this subsection, the numerical investigations of flow past an equilateral cylinder with different incidences are performed at $Re=100$ and 150. The Reynolds number is based on the free-stream velocity and the side of triangular cylinder. The mesh systems used for computation are illustrated in Figure 10 in close view. The number of nodes that are uniformly distributed over one unit length of a cylinder surface is to be 61 for all cases. Through a number of grid refinement studies, we consider that the grid systems for the calculations can result in satisfactory accurate solutions.

5.3.1. Flow pattern. As the flow becomes unsteady at Reynolds number up to 100, we visualize the flow field around the cylinder by the help of instantaneous streamlines for seven successive moments of time that span over a complete cycle of vortex shedding. As shown at the left side in Figures 11–15, the plots are for the cases of $\alpha=0°, 15°, 30°, 45°,\ 60°$. The sequence of streamlines clearly described the process of vortices formation and shedding from a triangular cylinder at different incidence angles. From these figures, we can observe that two critical points of streamline patterns described by Perry *et al.* [46], namely, the saddle and center are simultaneously born behind the cylinder, then moved to downstream, approached to each other and finally disappeared in the wake before a new vortex is shed. As further seen by the comparison of these figures, the variety in angle of incidence has significant influence on the flow pattern near the cylinder. In the case of $\alpha=0°$ ($Re=100$) with only one side facing the flow, at the reference time $t=t_0$, the larger and smaller vortices originally formed respectively from the upper and lower side of the cylinder, with the smaller is located near the rear corner of the cylinder. At time $t=t_0+1/6T$, these two counter-rotating vortices combined into a more larger one, and another new vortex appeared at the front lower corner of the cylinder, simultaneously. From $t_0+2/6T$ to $t_0+3/6T$, the combined vortex is separated from the cylinder and shed in the wake; at the same time, the vortex located at the lower side is growing gradually with the newly emerged vortex at the rear corner of the cylinder. The flow patterns shown in left plots of Figure 11(a) and (d), which are symmetric to each other about the stream centerline, indicate that $t_0+3/6T$ is the starting point of the second

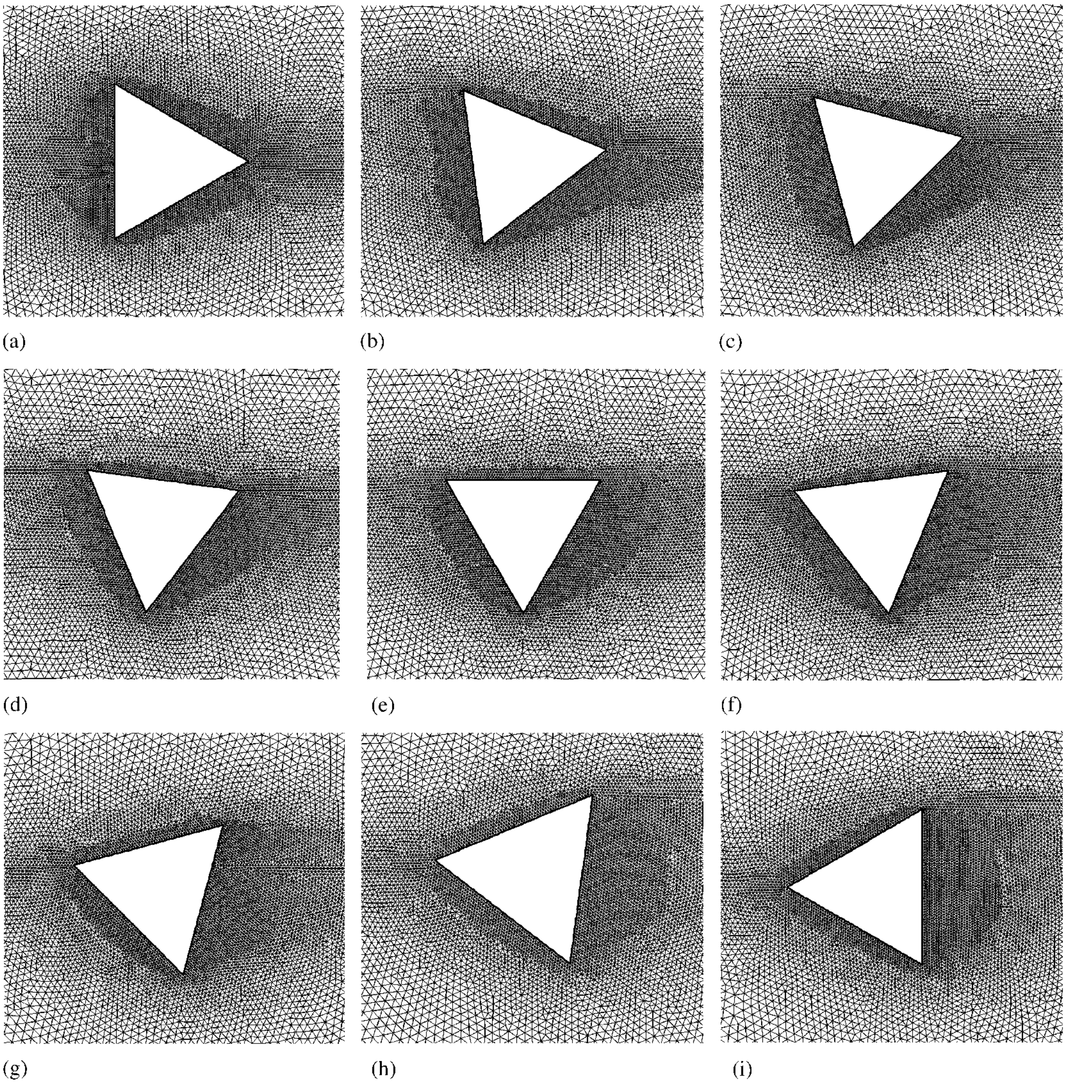

Figure 10. View of close-up mesh: (a) 26 949 nodes and 53 468 elements, $\alpha=0°$; (b) 27 101 nodes and 53 772 elements, $\alpha=7.5°$; (c) 26 868 nodes and 53 306 elements, $\alpha=15°$; (d) 27 408 nodes and 54 386 elements, $\alpha=22.5°$; (e) 27 265 nodes and 54 100 elements, $\alpha=30°$; (f) 27 488 nodes and 54 546 elements, $\alpha=37.5°$; (g) 26 945 nodes and 53 459 elements, $\alpha=45°$; (h) 27 537 nodes and 54 644 elements, $\alpha=52.5°$; and (i) 27 607 nodes and 54 784 elements, $\alpha=60°$.

half period time. In this time period, from $t_0+3/6T$ to t_0+T, a symmetric flow pattern to the first half period around the cylinder is observed clearly. From Figure 11(g), we can see that the next new cycle of vortex shedding begins at $t=t_0+T$, since the flow pattern exactly repeated them at $t=t_0$. It is observed from Figure 12 that, in the case of $\alpha=15°$, the most different feature from the above case is that the vortex born in the second half period is no longer symmetry to

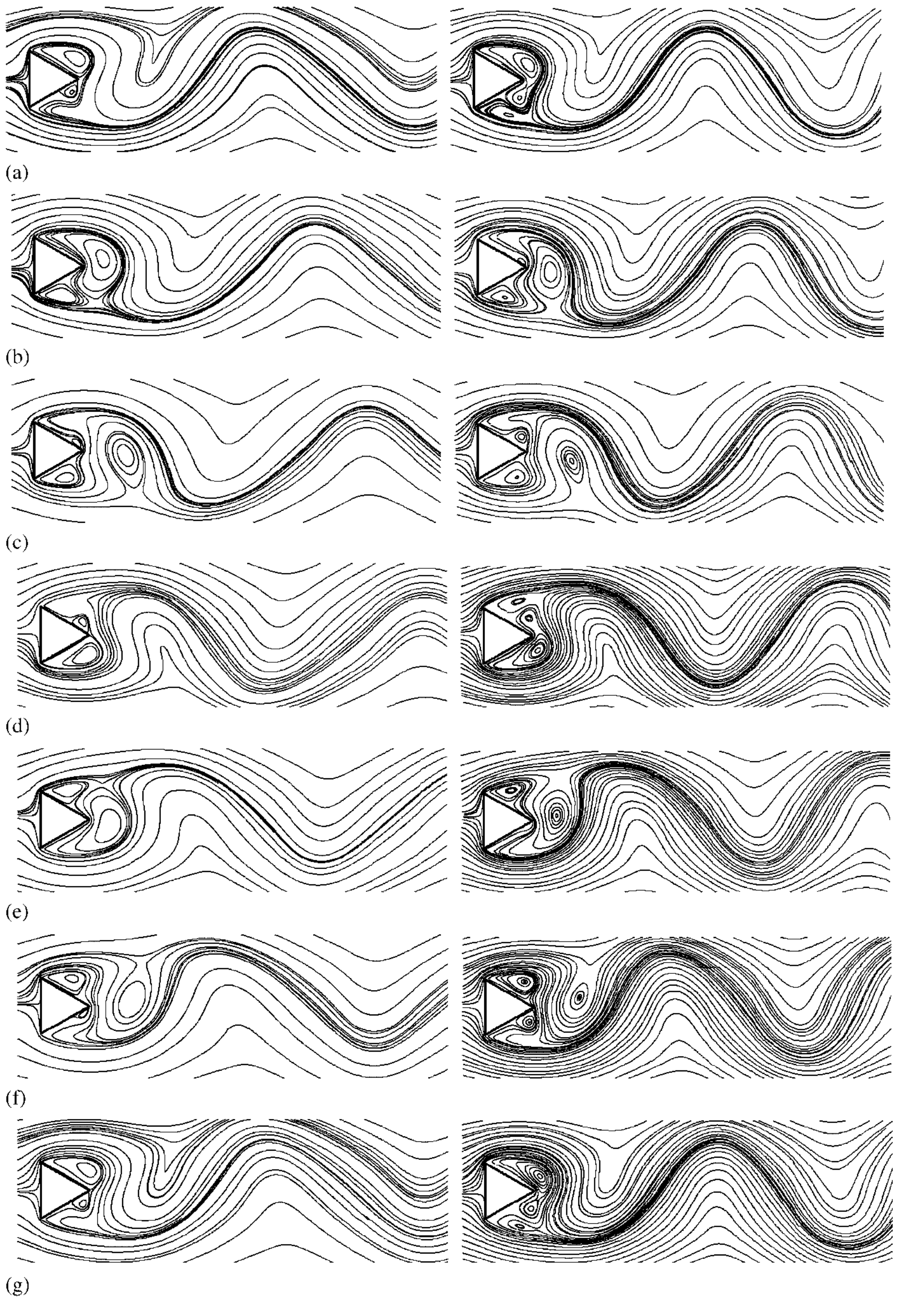

Figure 11. Time histories of streamlines behind a triangular cylinder with incidence angle of 0° at $Re=100$ (left) and $Re=150$ (right) for seven successive moments of time over a period of vortex shedding. t_0 is a reference dimensionless time, and for $Re=100$, 150, T is different period time calculated from Lift coefficient time history: (a) $t=t_0$; (b) $t=t_0+1/6T$; (c) $t=t_0+2/6T$; (d) $t=t_0+3/6T$; (e) $t=t_0+4/6T$; (f) $t=t_0+5/6T$; and (g) $t=t_0+T$.

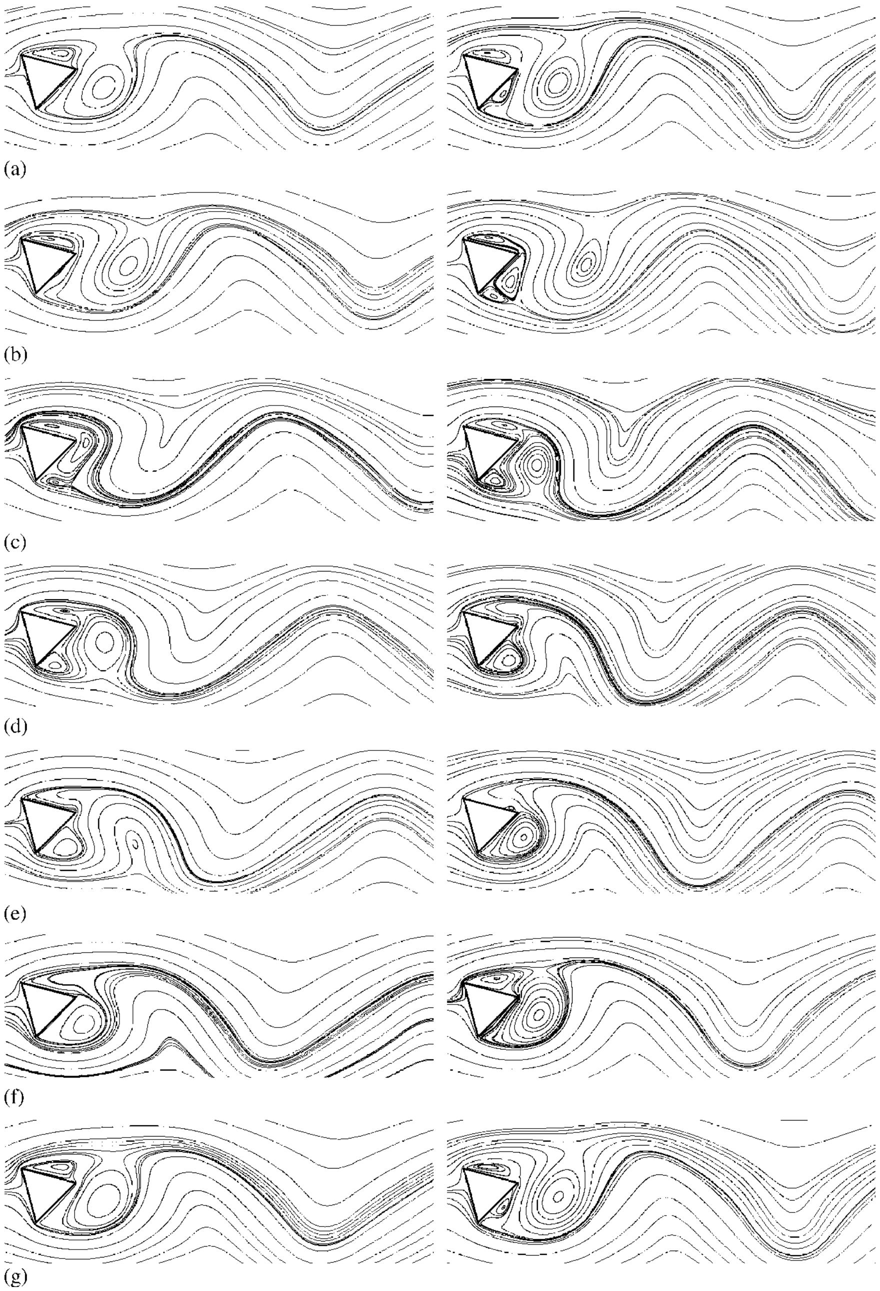

Figure 12. Time histories of streamlines behind a triangular cylinder with incidence angle of 15° at $Re = 100$ (left) and $Re = 150$ (right) for seven successive moments of time over a period of vortex shedding. t_0 is a reference dimensionless time, and for $Re = 100$, 150, T is different period time calculated from Lift coefficient time history: (a) $t = t_0$; (b) $t = t_0 + 1/6T$; (c) $t = t_0 + 2/6T$; (d) $t = t_0 + 3/6T$; (e) $t = t_0 + 4/6T$; (f) $t = t_0 + 5/6T$; and (g) $t = t_0 + T$.

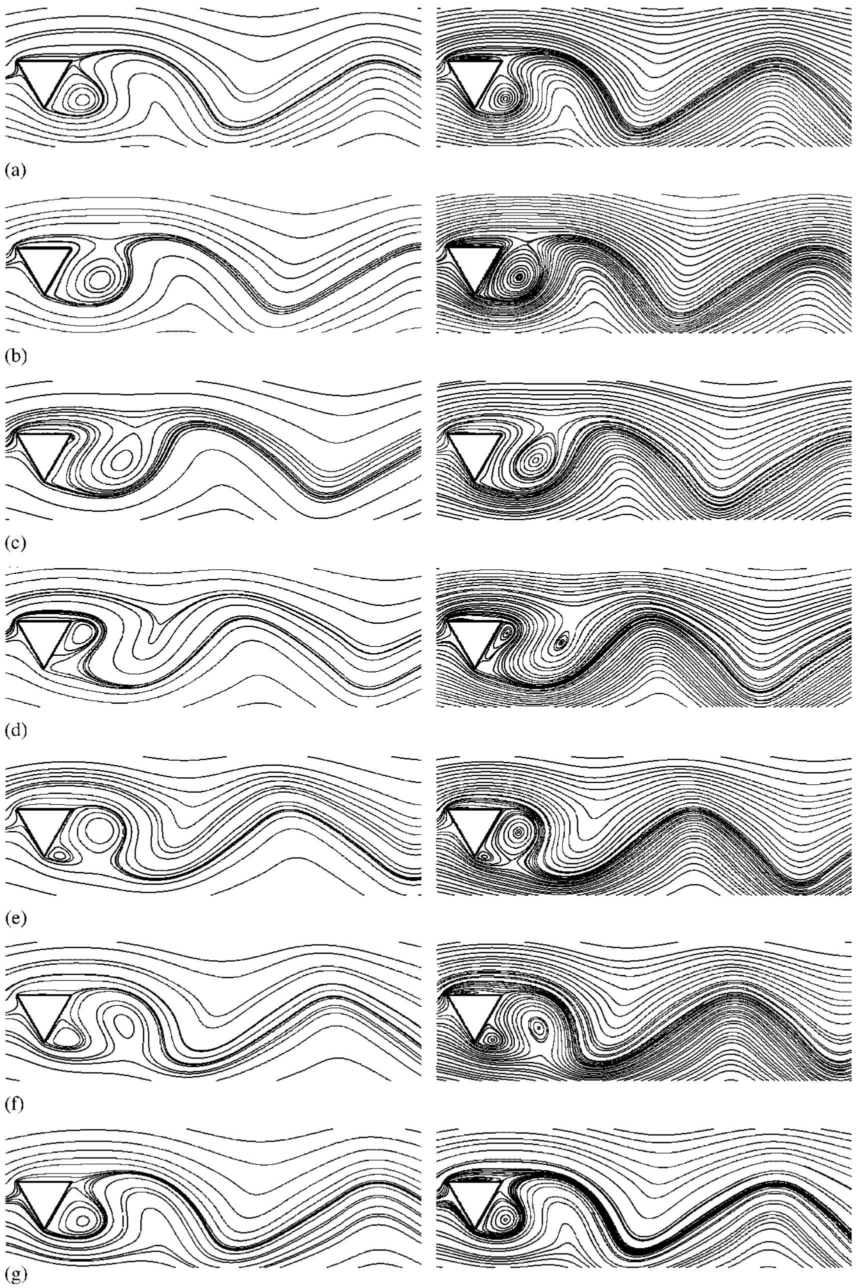

Figure 13. Time histories of streamlines behind a triangular cylinder with incidence angle of 30° at $Re=100$ (left) and $Re=150$ (right) for seven successive moments of time over a period of vortex shedding. t_0 is a reference dimensionless time, and for $Re=100$, 150, T is different period time calculated from Lift coefficient time history: (a) $t=t_0$; (b) $t=t_0+1/6T$; (c) $t=t_0+2/6T$; (d) $t=t_0+3/6T$; (e) $t=t_0+4/6T$; (f) $t=t_0+5/6T$; and (g) $t=t_0+T$.

DOI: 10.1002/fld

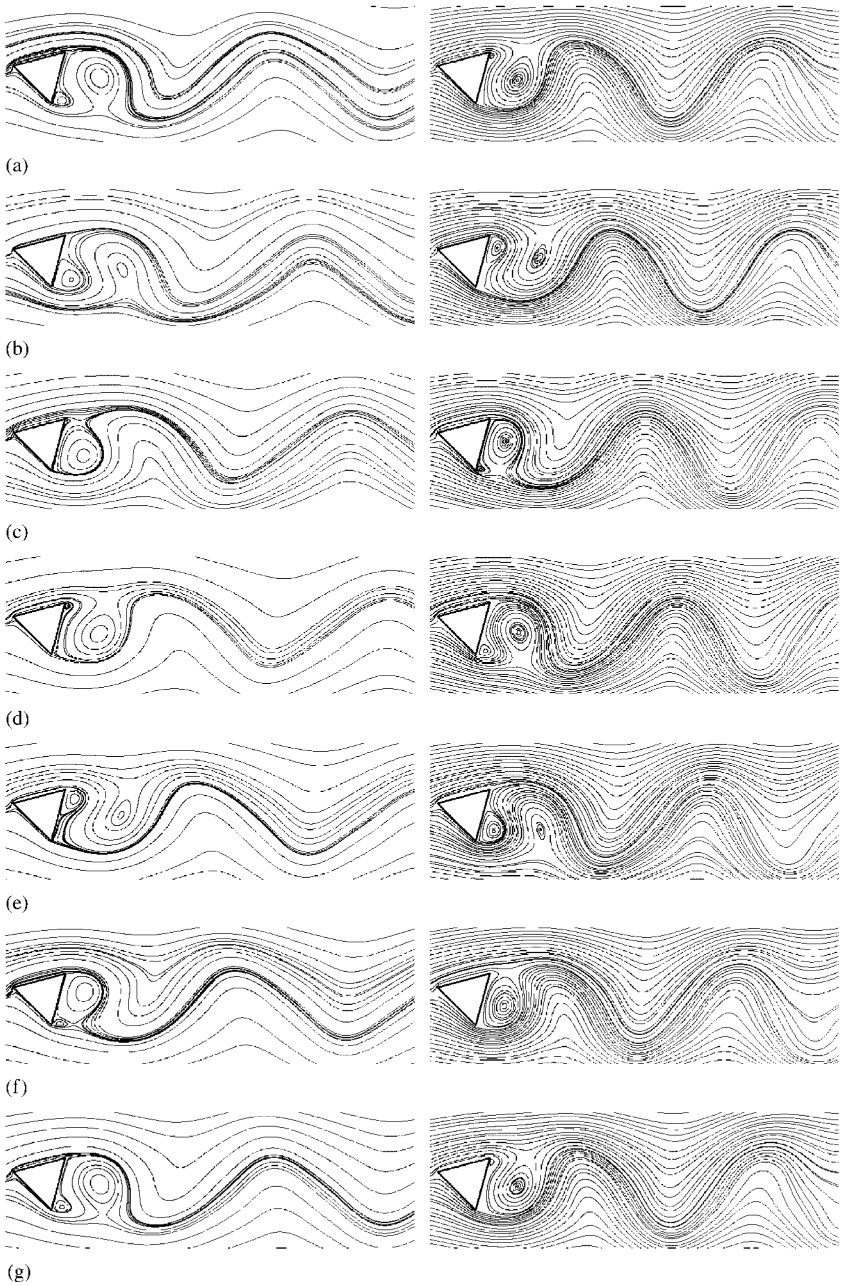

Figure 14. Time histories of streamlines behind a triangular cylinder with incidence angle of 45° at $Re = 100$ (left) and $Re = 150$ (right) for seven successive moments of time over a period of vortex shedding. t_0 is a reference dimensionless time, and for $Re = 100$, 150, T is different period time calculated from Lift coefficient time history: (a) $t = t_0$; (b) $t = t_0 + 1/6T$; (c) $t = t_0 + 2/6T$; (d) $t = t_0 + 3/6T$; (e) $t = t_0 + 4/6T$; (f) $t = t_0 + 5/6T$; and (g) $t = t_0 + T$.

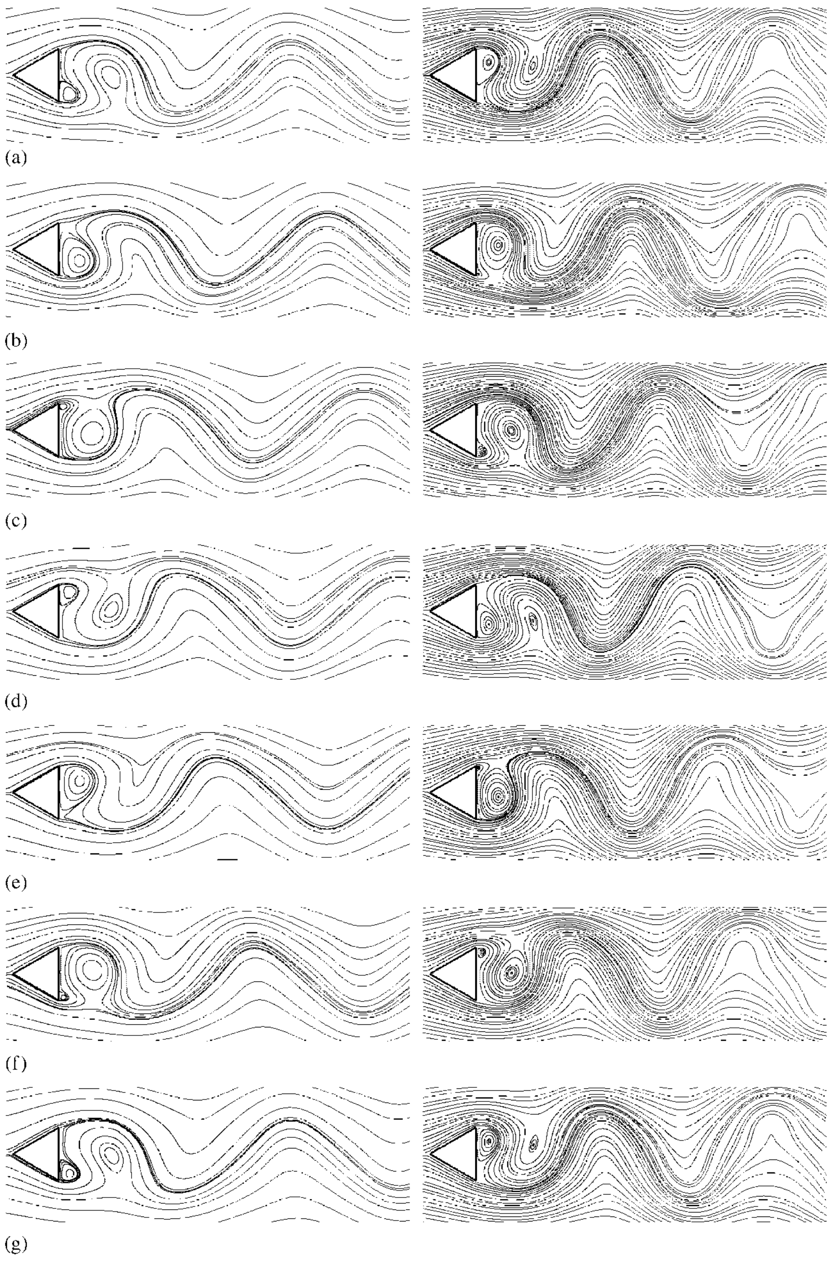

Figure 15. Time histories of streamlines behind a triangular cylinder with incidence angle of 60° at $Re = 100$ (left) and $Re = 150$ (right) for seven successive moments of time over a period of vortex shedding. t_0 is a reference dimensionless time, and for $Re = 100$, 150, T is different period time calculated from Lift coefficient time history: (a) $t = t_0$; (b) $t = t_0 + 1/6T$; (c) $t = t_0 + 2/6T$; (d) $t = t_0 + 3/6T$; (e) $t = t_0 + 4/6T$; (f) $t = t_0 + 5/6T$; and (g) $t = t_0 + T$.

the vortex in the first half period, due to the non-symmetric incidence of cylinder in the flow. We also found, for $\alpha = 15°$ at $Re = 100$, the two vortices of different shape and size formed at the upper and lower side of cylinder, and shed into the wake alternately. In the case of $\alpha = 60°$, the cylinder is placed such that its two sides face the free stream and its position is symmetric about the direction of the stream, as shown in Figure 15. From Figure 15, we can see that the flow pattern is clearly different from those in the previous cases. Owing to its streamlined shape, two vortices are always generated at the rear-end corners of the cylinder, and shed alternately in the wake, and during the first and second half period time, the flow pattern is symmetry to each other about the stream centerline, as found for $\alpha = 0°$. The same features of vortex formation and vortex shedding have been found for $\alpha = 45°$ from Figure 14. However, in this case, the flow in the first and second half periods becomes not symmetric any more. The result at $\alpha = 30°$ (see Figure 13) in which one side of cylinder is parallel to the direction of stream and another side faces the flow stream reveals that two vortices are also generated at the rear-end corners, as those in the cases of $\alpha = 45°,\ 60°$.

For the cases of Reynolds number equal to 150, the same mechanism and features of vortex shedding can be found from the right plots of Figures 11–15 as those of lower *Re* with equal incidence angle. It should be noted that for $\alpha = 30°$ ($Re = 150$), as shown in the right plots of Figure 13, the separation occurs at the leading edge with reattachment on the top face of the cylinder, which is different from the case of $Re = 100$. Such phenomena are not found when incidence angle is larger than 30° for $Re = 150$.

5.3.2. Force coefficients and Strouhal number. Figure 16 shows the time-dependent histories of the Drag and Lift coefficients on the surface of the cylinder for different incidence angles at $Re = 100$. They all demonstrate clear periodicity, which implies again the periodic vortex shedding behind the cylinder. However, when the cylinder is inclined at some angle (i.e. $0° < \alpha < 60°$), the oscillation manner of Drag coefficient around its mean value is different from those in the non-inclined cases ($\alpha = 0°, 60°$). For further illustration, we show the result for spectral analysis on the signals at $\alpha = 0°,\ 30°,\ 52.5°$ and $60°$ in Figure 17. We can observe that in the inclined cases ($\alpha = 30°, 52.5°$), the oscillation of Drag coefficient has two frequency components, i.e. for $\alpha = 30°$, the dominating primary frequency $f_s = 0.174$ and the secondary frequency $f_s = 0.348$; for $\alpha = 52.5°$, the primary frequency $f_s = 0.194$ and the secondary frequency $f_s = 0.388$. Clearly, the secondary frequency is twice as that of the primary frequency, while the Lift coefficient signal of oscillating frequencies for $\alpha = 30°$ and $52.5°$ are 0.174 and 0.194, respectively, which are equal to the corresponding primary frequencies of Drag signals. At $\alpha = 0°,\ 60°$ a single dominant frequency of Drag coefficient has been seen to be twice as that of the Lift coefficient. When incidence is equal to 60°, the same behavior is also observed in the simulations by De and Dalal [47]. Variation of Strouhal number with incidence angle has been shown in Figure 18(a). At $Re = 100$, the frequency of vortex shedding increases with incidence angle in the range of $0° \leqslant \alpha \leqslant 60°$. The increase in incidence angle at around $\alpha = 30°$ causes the curve to increase at a quicker rate and reaches its flat maximum at $\alpha = 60°$, while its minimum value happens at $\alpha = 0°$. However, at $Re = 150$, the Strouhal number has a maximum at $\alpha = 45°$ and decreases slightly for higher incidence angle ($45° < \alpha < 60°$). The influences of incidence on mean value of Drag coefficient ($\bar{C}_D$) and rms value of Lift coefficient (C_{Lrms}) at $Re = 100$ and 150 are depicted in Figure 18(b). It can be seen from Figure 18(b) that, in the range of $0° \leqslant \alpha \leqslant 30°$, $\bar{C}_D$ decreases from the maximum value, which happens at $\alpha = 0°$, with increasing α until its minimum value is reached at $\alpha = 30°$. After this minimum is achieved, the

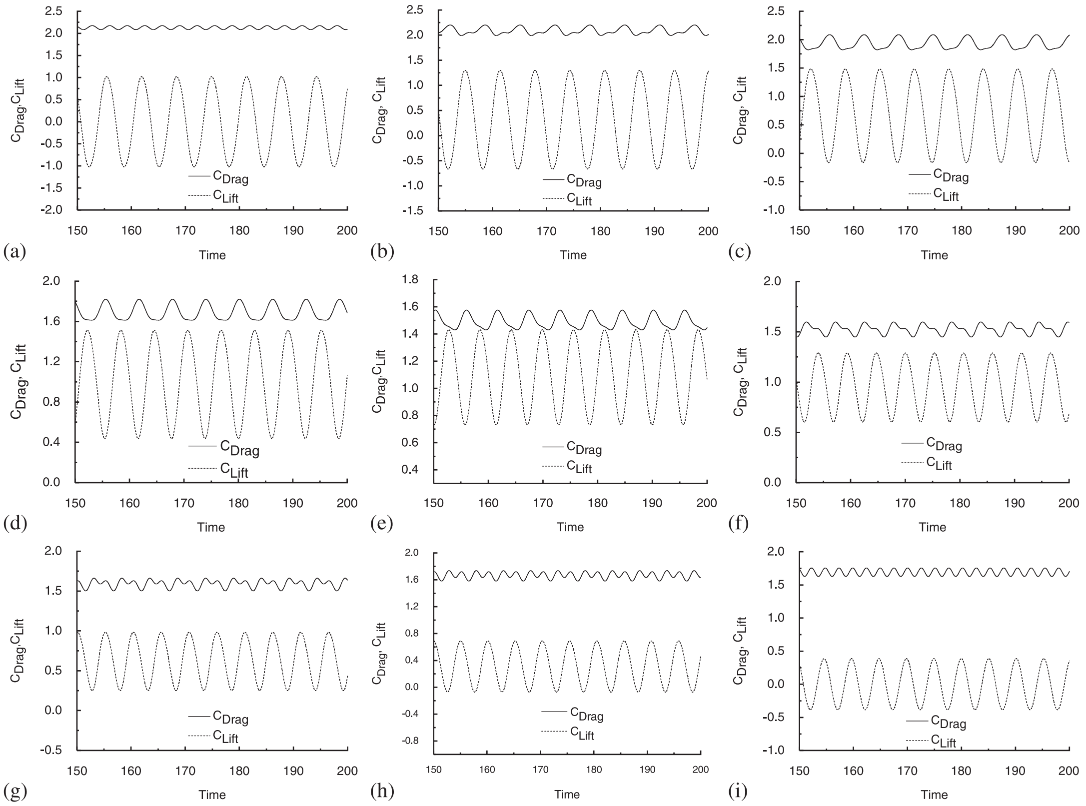

Figure 16. Time histories of Drag and Lift coefficients of flow past a triangular cylinder with different incidence angles at $Re=100$: (a) $\alpha=0°$; (b) $\alpha=7.5°$; (c) $\alpha=15°$; (d) $\alpha=22.5°$; (e) $\alpha=30°$; (f) $\alpha=37.5°$; (g) $\alpha=45°$; (h) $\alpha=52.5°$; and (i) $\alpha=60°$.

value of $\bar{C}_D$ goes slightly up with α. The contrary behavior is observed for the influence of α on C_{Lrms}. C_{Lrms} reaches its maximum value at $\alpha=30°$, and then falls off with the increase in α and finally reaches the minimum at $\alpha=60°$.

6. CONCLUSIONS

In this paper, a two-step TCBG algorithm is developed, which is based on the introduction of two-step second-order Taylor series expansion along the characteristic of the momentum equation. The calculation of pressure is separated from that of the velocity, by solving the Poisson equation for pressure, which is derived from the Crank–Nicolson scheme of the momentum equation. Consequently, the splitting error is circumvented, which will occur in the classical CBS method. The tests on some benchmark examples have demonstrated the effectiveness of the proposed method for the solution of incompressible flow and showed its more numerical accuracy with less numerical dissipative character.

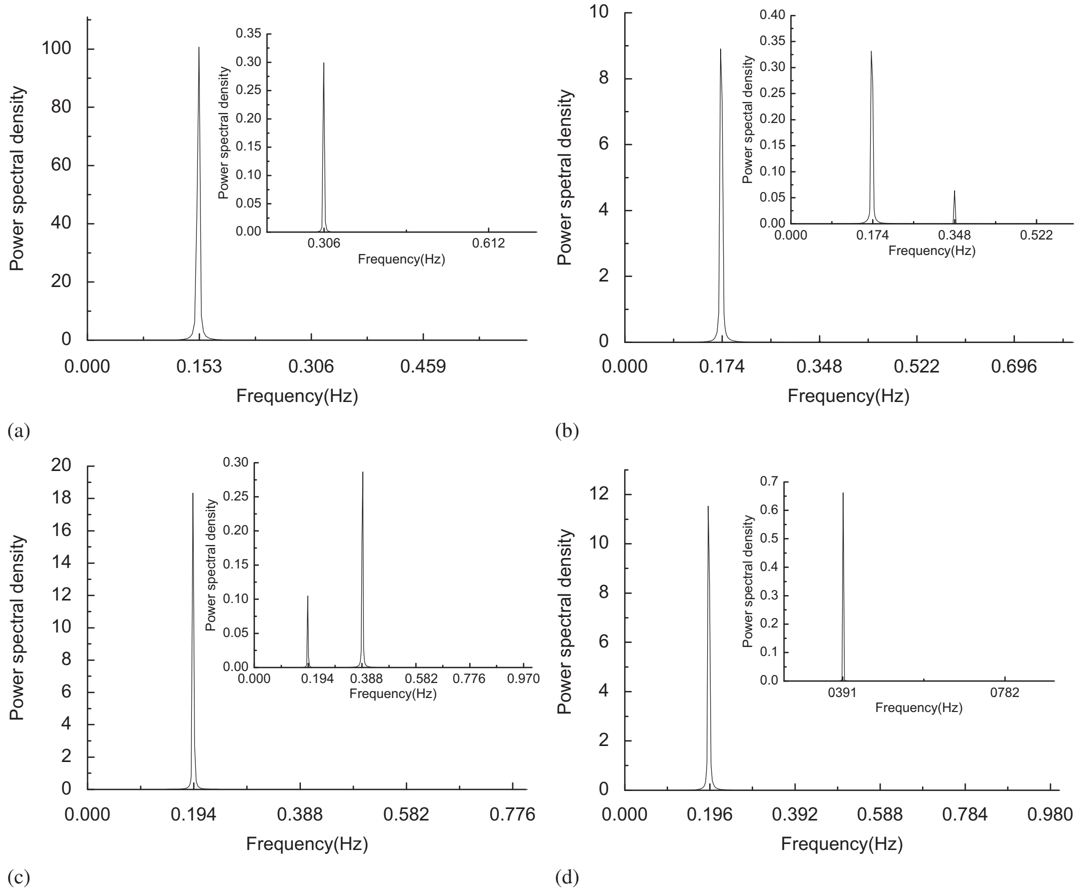

(a) (b) (c) (d)

Figure 17. Fundamental frequency of Lift and Drag coefficients (shown in the inset) signals at different incident angles ($Re=100$): (a) $\alpha=0°$; (b) $\alpha=30°$; (c) $\alpha=52.5°$; and (d) $\alpha=60°$.

The developed algorithm is employed to simulate unconfined flow around triangular cylinder with different incidence angles at low Reynolds numbers. The visualization of numerical solution is realized by the instantaneous streamlines. It shows that incidence angle has significant effect on the flow patterns around the triangular cylinder. The influence of incidence on some flow parameters such as Strouhal number, mean value of Drag coefficient and rms value of Lift coefficient is studied quantitatively. The results show that for the considered Reynolds number, the Strouhal number increases generally with the increase in incidence angle; the mean value of Drag coefficient and the rms value of Lift coefficient reach respectively its minimum and maximum at the incidence of 30°; in this case, one of the sides of triangular cylinder is parallel to the free stream.

Through the analysis on the signals of Drag coefficient, we can also conclude that if the triangular cylinder is located non-symmetrically to the free stream, the oscillation of Drag coefficient has two frequency components, and its primary frequency is half of the secondary frequency and is equal

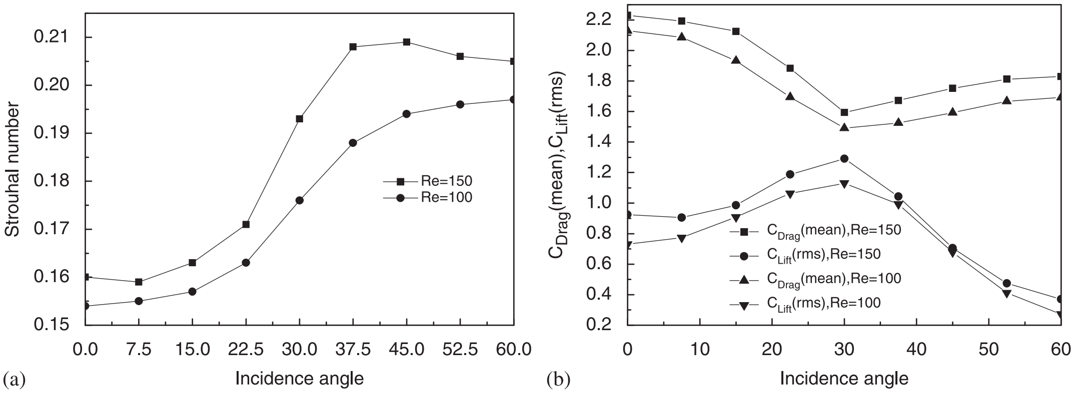

Figure 18. (a) Incidence angle (degree) versus Strouhal number and (b) incidence angle (degree) versus mean value of Drag coefficient and rms value of Lift coefficient at $Re = 100$, 150.

to the frequency of Lift coefficient, while only single frequency dominates the Drag oscillation for flow past symmetrically located cylinder.

ACKNOWLEDGEMENTS

Support from the Key Project Foundation of Science and Technology Development of Shanghai (No. 07JC14023) and the National Natural Science Foundation of China (Project No. 50778111) are acknowledged.

REFERENCES

1. Hughes TJR, Franca LP, Balestra M. A new finite element formulation for computational fluid dynamics: V. Circumventing the Babuska–Brezzi condition: a stable Petrov–Galerkin formulation of the Stokes problem accommodating equal-order interpolations. *Computer Methods in Applied Mechanics and Engineering* 1986; **59**:85–99.
2. Tezduyar TE, Mittal S, Ray SE, Shih R. Incompressible flow computations with stabilized bilinear and linear equal-order-interpolation velocity–pressure elements. *Computer Methods in Applied Mechanics and Engineering* 1992; **95**:221–242.
3. Tezduyar TE, Behr M, Liou J. A new strategy for finite element computations involving moving boundaries and interfaces—the deforming-spatial-domain/space–time procedure: I. The concept and the preliminary numerical tests. *Computer Methods in Applied Mechanics and Engineering* 1992; **94**:339–351.
4. Onate E. A stabilized finite element method for incompressible viscous flows using a finite increment calculus formulation. *Computer Methods in Applied Mechanics and Engineering* 2000; **182**:355–370.
5. Codina R, Blasco J. Stabilized finite element method for the transient Navier–Stokes equations based on a pressure gradient projection. *Computer Methods in Applied Mechanics and Engineering* 2000; **182**:277–300.
6. Brooks AN, Hughes TJR. Streamline Upwind/Petrov–Galerkin formulations for convective dominated flows with particular emphasis on the incompressible Navier–Stokes equations. *Computer Methods in Applied Mechanics and Engineering* 1982; **32**:199–259.
7. Hughes TJR, Franca LP, Hulbert GM. A new finite element formulation for computational fluid dynamics: VIII. The Galerkin/least-squares method for advective–diffusive equations. *Computer Methods in Applied Mechanics and Engineering* 1989; **73**:173–189.
8. Hughes TJR. Multiscale phenomena: Green's function, the Dirichlet-to-Neumann formulation, subgrid scale models, bubbles and the origins of stabilized formulations. *Computer Methods in Applied Mechanics and Engineering* 1995; **127**:387–401.

9. Donea J. A Taylor–Galerkin method for convection transport problems. *International Journal for Numerical Methods in Engineering* 1984; **20**:101–119.
10. Douglas J, Russell TF. Numerical methods for convection dominated diffusion problems based on combining the method of characteristics with finite element or finite difference procedures. *SIAM Journal on Numerical Analysis* 1982; **19**:871–885.
11. Zienkiewicz OC, Codina R. A general algorithm for compressible and incompressible flow, part I: the split, characteristic-based scheme. *International Journal for Numerical Methods in Fluids* 1995; **20**:869–885.
12. Chorin AJ. A numerical method for solving incompressible viscous problems. *Journal of Computational Physics* 1967; **2**:12–26.
13. Témam R. Sur l'approximation de la solution des équations de Navier–Stokes par la méthode des pas fractionnaires (II). *Archives for Rational Mechanics and Analysis* 1969; **33**:377–385.
14. Zienkiewicz OC, Ortiz P. A split-characteristic based finite element model for the shallow water equations. *International Journal for Numerical Methods in Engineering* 1995; **20**:1061–1080.
15. Zienkiewicz OC, Nithiarasu P, Codina R, Vázquez M, Ortiz P. The characteristic-based-split procedure: an efficient and accurate algorithm for fluid problems. *International Journal for Numerical Methods in Fluids* 1999; **31**:359–392.
16. Zienkiewicz OC, Satya Sai BVK, Morgan K, Codina R, Vázquez M. A general algorithm for compressible and incompressible flow, part II: tests on the explicit form. *International Journal for Numerical Methods in Fluids* 1995; **20**:887–913.
17. Codina R, Vázquez M, Zienkiewicz OC. General algorithm for compressible and incompressible flows, part III: a semi-implicit form. *International Journal for Numerical Methods in Fluids* 1998; **27**:12–32.
18. Zienkiewicz OC, Satya Sai BVK, Morgan K, Codina R. Split characteristic based semi-implicit algorithm for laminar/turbulent incompressible flows. *International Journal for Numerical Methods in Fluids* 1996; **23**:787–809.
19. Nithiarasu P, Zienkiewicz OC. On stabilization of the CBS algorithm. Internal and external time steps. *International Journal for Numerical Methods in Engineering* 2000; **48**:875–880.
20. Nithiarasu P. On boundary conditions of the characteristic based split (CBS) algorithm for fluid dynamics. *International Journal for Numerical Methods in Engineering* 2002; **54**:523–536.
21. Zienkiewicz OC, Nithiarasu P. A universal algorithm for fluid dynamics. The Characteristic Based Split (CBS) procedure. Some tests on stability and boundary conditions. *Archives of Mechanics* 2000; **52**:857–887.
22. Nithiarasu P, Codina R, Zienkiewicz OC. The Characteristic-Based Split (CBS) scheme—a unified approach to fluid dynamics. *International Journal for Numerical Methods in Engineering* 2006; **6**:1514–1546.
23. Nithiarasu P, Zienkiewicz OC. Analysis of an explicit and matrix free fractional step method for incompressible flows. *Computer Methods in Applied Mechanics and Engineering* 2006; **195**:5537–5551.
24. Nithiarasu P. An efficient artificial compressibility (AC) scheme based on the characteristic based split (CBS) method for incompressible flows. *International Journal for Numerical Methods in Engineering* 2003; **56**: 1815–1845.
25. Thomas CG, Nithiarasu P. Effect of variable smoothing and stream line direction on the viscous compressible flow calculations. *International Journal of Numerical Methods for Heat and Fluid Flow* 2005; **15**:420–428.
26. Nithiarasu P, Mathur JS, Weatherill NP, Morgan K. Three-dimensional incompressible flow calculations using the characteristic based split (CBS) scheme. *International Journal for Numerical Methods in Fluids* 2004; **44**:1207–1229.
27. Nithiarasu P, Liu CB. Steady and unstable flow calculations in a double driven cavity using the explicit CBS scheme. *International Journal for Numerical Methods in Engineering* 2005; **63**:380–397.
28. Sai BVKS, Zienkiewicz OC, Manzari MT, Lyra PRM, Morgan K. General purpose vs special algorithms for high speed flows with shocks. *International Journal for Numerical Methods in Fluids* 1998; **27**:57–80.
29. Nithiarasu P, Zienkiewicz OC, Sai BVKS, Morgan K, Codina R, Vázquez M. Shock capturing viscosities for the general fluid mechanics algorithm. *International Journal for Numerical Methods in Fluids* 1998; **28**:1325–1353.
30. Nithiarasu P. An arbitrary Eulerian Lagrangian (ALE) method for free surface flow calculations using the characteristic based split (CBS) scheme. *International Journal for Numerical Methods in Fluids* 2005; **48**: 1415–1428.
31. Nithiarasu P, Liu CB. An artificial compressibility based characteristic based split (CBS) scheme for steady and unsteady turbulent incompressible flows. *Computer Methods in Applied Mechanics and Engineering* 2006; **195**:2961–2982.
32. Morandi-Cecchi M, Venturin M. Characteristic-based split (CBS) algorithm finite element modelling for shallow waters in the Venice lagoon. *International Journal for Numerical Methods in Engineering* 2006; **66**:1641–1657.

DOI: 10.1002/fld

33. Nithiarasu P, Massarotti N, Mathur JS. Forced convection heat transfer from solder balls on a printed circuit board using the characteristic based split (CBS) scheme. *International Journal of Numerical Methods for Heat and Fluid Flow* 2005; **15**:73–95.
34. Massarotti N, Nithiarasu P, Zienkiewicz OC. Characteristic-based-split (CBS) algorithm for incompressible flow problems with heat transfer. *International Journal of Numerical Methods for Heat and Fluid Flow* 1998; **8**(8):969–990.
35. Salomoni VA, Schrefler BA. A CBS-type stabilizing algorithm for the consolidation of saturated porous media. *International Journal for Numerical Methods in Engineering* 2005; **63**:502–527.
36. Salomoni VA, Schrefler BA. Stabilized-coupled modelling of creep phenomena for saturated porous media. *International Journal for Numerical Methods in Engineering* 2006; **66**:1587–1617.
37. Massarotti N, Nithiarasu P, Zienkiewicz OC. Natural convection in porous medium—fluid, interface problems. A finite element analysis by using the CBS procedure. *International Journal of Numerical Methods for Heat and Fluid Flow* 2001; **11**:473–490.
38. Massarotti N, Nithiarasu P, Carotenuto A. Microscopic and macroscopic approach for natural convection in enclosures filled with fluid saturated porous medium. *International Journal of Numerical Methods for Heat and Fluid Flow* 2003; **13**:862–886.
39. Liu CB, Nithiarasu P. The characteristic-based split (CBS) scheme for viscoelastic flow past a circular cylinder. *International Journal for Numerical Methods in Fluids* 2008; **57**:157–176.
40. Zienkiewicz OC, Rojek J, Taylor RL, Pastor M. Triangles and tetrahedra in explicit dynamic codes for solids. *International Journal for Numerical Methods in Engineering* 1999; **43**:565–583.
41. Rojek J, Zienkiewicz OC, Onate E, Postek E. Advances in FE explicit formulation for simulation of metal forming processes. *Journal of Materials Processing Technology* 2001; **119**(1–3):41–47.
42. Codina R, Badia S. On some pressure segregation methods of fractional-step type for the finite element approximation of incompressible flow problems. *Computer Methods in Applied Mechanics and Engineering* 2006; **195**:2900–2918.
43. Guermond JL, Quartapelle L. On stability and convergence of projection methods based on pressure Poisson equation. *International Journal for Numerical Methods in Fluids* 1998; **26**:1039–1053.
44. Zienkiewicz OC, Taylor RL. *The Finite Element Method*, *Volume 3*: *Fluid Dynamics* (5th edn). Butterworth-Heinemann: Oxford, 2000.
45. Erturk E, Corke TC, Gokcol C. Numerical solutions of 2-D steady incompressible driven cavity flow at high Reynolds numbers. *International Journal for Numerical Methods in Fluids* 2005; **48**:747–774.
46. Perry AE, Chong MS, Lim TT. The vortex shedding process behind two-dimensional bluff bodies. *Journal of Fluid Mechanics* 1982; **116**:77–90.
47. De AK, Dalal A. Numerical simulation of unconfined flow past a triangular cylinder. *International Journal for Numerical Methods in Fluids* 2006; **52**:801–821.

DOI: 10.1002/fld